International Journal of Hydrogen Energy 77 (2024) 193–202

Contents lists available at ScienceDirect

International Journal of Hydrogen Energy

journal homepage: www.elsevier.com/locate/he

2D nanosheet SnS_2 solution-processed photoanodes: Unveiling enhanced visible light absorption for solar fuels applications

Yudania Sánchez [a], Maxim Guc [a], Sara Martí-Sánchez [b], Maykel Jiménez-Guerra [a,c], Shadai Lugo-Loredo [d], Jordi Arbiol [e], Alejandro Perez-Rodriguez [a,f], Jordi Martorell [g,h], Carles Ros [h,*]

[a] Catalonia Institute for Energy Research (IREC), Jardins de les Dones de Negre 1, 08930 Sant Adrià del Besòs, Barcelona, Spain
[b] Catalan Institute of Nanoscience and Nanotechnology (ICN2), CSIC and BIST, Campus UAB, Bellaterra, 08193, Barcelona, Catalonia, Spain
[c] Escola d'Enginyeria de Barcelona Est (EEBE), Universitat Politècnica de Catalunya, Av. Eduard Maristany, 16, 08019, Barcelona, Spain
[d] Universidad Autónoma de Nuevo León, (UANL), Facultad de Ciencias Químicas, Av. Universidad, Cd. Universitaria, San Nicolás de los Garza, Nuevo León, 66455, Mexico
[e] ICREA, Pg. Lluís Companys 23, 08010, Barcelona, Catalonia, Spain
[f] Departament d'Enginyeria Electrònica i Biomèdica, Universitat de Barcelona (UB), Martí i Franquès 1, 08028, Barcelona, Spain
[g] Departament de Física, Universitat Politècnica de Catalunya (UPC), 08222, Terrassa, Spain
[h] Institut de Ciencies Fotoniques (ICFO), The Barcelona Institute of Science and Technology (BIST), 08860, Castelldefels, Spain

ARTICLE INFO

Handling Editor: Ibrahim Dincer

Keywords:
SnS_2
Chemical bath deposition
Photoelectrochemical water splitting
Hydrogen
Nanosheets

ABSTRACT

The scale-up of photoelectrochemical water splitting and CO_2 reduction is currently hindered by the excessive band gap of metal oxide photoanodes. Metal sulfides 2D nanostructured morphology offer improved optoelectronic properties and catalytic capabilities in the oxygen evolution reaction (OER). This study demonstrates for the first time visible spectra absorption capabilities of Sn_xS_y photoanodes, fabricated by facile non-vacuum techniques and post-annealed in a sulfur atmosphere, yielding SnS_2 multilayer nanosheets with visible-light absorption down to 900 nm wavelengths. Optimal annealing (500 °C) resulted in >1 V photovoltages, photocurrents surpassing 1.6 mA/cm^2 at 1.23V_{RHE}, incident photon-to-current conversion efficiency (IPCE) of 75% at 330 nm. Photon conversion in the 500–900 nm range (down to 1.37 eV) is correlated with phase transformation from orthorhombic α-SnS to Sn_2S_3 and further hexagonal SnS_2. IPCE is key for describing effective phase transformation and photon conversion at wavelengths below the dominant direct band gap for the SnS_2, suggesting potential indirect transitions or confinement in the low-dimensional nanosheets. SnS_2 nanosheets fabricated by solution-processed means, hold great potential for large-scale, cost-effective, and efficient photoelectrochemical devices.

1. Introduction

As we continue to search for clean and renewable sources of energy and new energy carriers, photoelectrochemical (PEC) water splitting [1] is emerging as a promising candidate for hydrogen production. Despite extensive research [2] being conducted in the pursuit of stable and efficient photoelectrodes [3], there is still a need for materials that can achieve efficient photon energy conversion and storage [4]. Short band gap absorbers, such as those used in photovoltaics (e.g. Si [5–9], GaAs [10–12], CIGS [13–17], and CZTS [18–24]), have been efficiently implemented in PEC with efficiencies close to those of PV, and many of them requiring extra layers to achieve stability (i.e. TiO2 protective layers [10,25–28] or heterojunctions [29,30] for photoanodes [10,28, 31–33] and photocathodes [6,30,34–36]) some of them offering also enhanced catalytic properties (i.e. NiOx protective layers [37–40], forming a NiOOH layered double hydroxide highly catalytic film [41, 42] if Fe impurities are added [43–45]). However, mid and large band gap materials that are suitable for tandem applications are difficult to find due to cost, lack of abundant materials, or low efficiency [46–49]. While TiO2 was the first metal oxide to be applied as a photoanode [50, 51], followed by shorter band gap candidates like Fe2O3 [52–54], WO3 [55,56], and BiVO4 [57–64], overall photocurrents are still not enough

* Corresponding author.
E-mail address: carles.ros@icfo.eu (C. Ros).

https://doi.org/10.1016/j.ijhydene.2024.06.160
Received 8 January 2024; Received in revised form 21 May 2024; Accepted 11 June 2024
Available online 17 June 2024

to match the necessary productivity of short band gap candidates. [51,65,66].

Recently, 2 dimensional atomically thin transition metal chalcogenides (TMCs) such as WS_2, WSe_2, MoS_2, and $MoSe_2$ have emerged [67] as efficient, tunable, low-cost materials for a broad range of optoelectronic devices [68] and for photoelectrochemical applications [69–72] thanks to the electronic confinement properties of low-dimensional morphologies in reducing the effective band gap and improving charge extraction and transport properties [73,74]. TMCs have also shown promising results for PEC [71,75–79], both as absorbers with shorter band gaps and as hydrogen and oxygen evolution reactions (HER and OER) catalysts [80–82]. Research has been devoted to metal mono-, di-, and tri-chalcogenides [83,84], most of which are fabricated by hydrothermal-based processes, obtaining photocurrents that outperform metal oxides. In thin film production, different chemical and physical deposition routes are used such as atomic layer deposition (ALD) [85], DC and RF magnetron sputtering [86–88], or chemical bath deposition (CBD). However, compared to ALD and sputtering, CBD is attracting significant interest because of its low cost, simplicity, uniformity, and ease of substrate choices [67,89]. Additionally, multiple samples can be fabricated in a single run nearly at room temperature and the control over the thickness and other physical and chemical properties of the film can be easily achieved by altering the growth parameters [89]. This technique is widely used to deposit interfacial buffer layers, such as CdS [25,90,91]. However, few articles have used CBD to fabricate these photoelectrodes [30,92,93] or to protect those with overlayers [94]. This under-appreciated technique provides accurate control of nanoscale-size thin films with facile low-temperature, solution-based depositions [95–97].

Among chalcogenides, tin sulfides (Sn_xS_y) have attracted attention in recent years due to the abundance of Sn and S, their fabrication simplicity [98–103], facets with enhanced photocatalytic activity [104], optoelectronic properties [99,105,106], noteworthy PV performance [107,108], semitransparency [67,109], and the possibility to form different crystallographic phases and stoichiometry by tuning the thermal sulfurization treatment [108,110]. Several studies have been conducted to investigate the PEC performance of SnS and its related phases, pointing out to its catalytic properties for water oxidation [82]. In 2018, Cao et al. fabricated an FTO/SnS/SnS_2/Pt photocathode that generated 26.7 μA/cm^2 at 1.23 V_{RHE} and was stable for a few minutes [111]. Zuo et al. fabricated a SnO_2–Pt photoanode with currents of around 0.12 mA/cm^2 in 2019. Same year, Joshi et al. tested also SnS_2 as a photoanode for iodine oxidation [106], and Lin et al. formed an heterojunction with hydrogenated TiO_2 to form a bias-free type-II photoanode [102]. In 2020, Hu et al. decorated AZO inverse opal spheres with SnS_2 to form photoanodes [103] that achieved ~1 mA/cm^2. Wu et al. deposited 2D SnS_2 flakes with high absorption on SnO_2 nanoflakes, and the heterojunction helped with an enhanced electrical field, reaching 0.7 mA/cm^2 [112]. That year, Wu et al. highlighted the infrared conversion capabilities of SnS_2/SnO_2 heterojunctions in photoanodic conditions [112]. In 2021, Osuagwu et al. used H_2S direct sulfidation of FTO substrates to form vertically aligned SnS_2 nanoflakes (NFs) that reached 60% IPCE at 460 nm wavelengths [113]. By hydrothermal means, Deng et al. fabricated SnS_2 photoanodes acting as photodetectors [99]. These studies have determined that the SnS_2 indirect bandgap is between 2.2 and 2.4 eV [98,102,103], demonstrating SnS_2 as a promising photoanode candidate for tandem PEC-PV with a bandgap absorption edge capable of absorbing a significant portion of blue light. SnS_2 has exhibited n-type semiconductor behavior and proper band alignment for water oxidation, but further research is needed on the crystallographic transition between SnS and SnS_2 linked to photon absorption and conversion capabilities.

In this work, SnS is grown using different CBD times on FTO, and the crystallographic phase transition upon annealing from 300 to 500 °C in a sulfur-rich atmosphere is studied by Raman spectroscopy and X-Ray diffractometry, and the complex microstructural morphology of the best-performing sample is analyzed by HRTEM. The photoelectrochemical capabilities of these materials while performing the water splitting's OER are analyzed, and changes in the optical and electronically active band gap are observed simultaneously to the SnS/Sn_2S_3/SnS_2 phase transition, presenting an improvement of several performance parameters with the formation of the hexagonal SnS_2 phase.

2. Materials and methods

Chemical deposition of the thin films was made on 2.5 × 2.5 cm and 2 mm thick FTO glass substrates, successively ultrasonically cleaned in acetone, isopropyl alcohol, and deionized water and dried with a nitrogen gun. The reagents used for the deposition of SnS thin films were: $SnCl_2$ (tin (II) chloride, 99.8%, Aldrich), $Na_2S_2O_3{\cdot}5H_2O$ (sodium thiosulphate pentahydrate, 99.5%, Aldrich), CH_4N_2S (thiourea, 99%, Aldrich), $Na_3C_6H_5O_7$ (sodium citrate, 99%, Serviquimia) and deionized water. The chemical bath contained 0.03 M of $SnCl_2$, 1 M $Na_2S_2O_3{\cdot}5H_2O$, 1 M CH_4N_2S, 1 M $Na_3C_6H_5O_7$, and deionized water to complete 100 mL. The glass substrates were horizontally placed in a temperature-controlled circulation chemical bath at 60 °C with 4 different deposition times, 1, 2, 4, and 6 h. Subsequently, the substrates were removed from the bath, washed with deionized water, and dried with a nitrogen gun. Then, the deposited layers were subjected to different thermal treatments of sulfurization in a tubular furnace (Hobersal, Spain). The samples are inserted into a graphite box (23 cm^3 free volume) with 100 mg of sulfur 5 N (Alfa Aesar) [114,115]. The different reactive annealing temperatures that were applied in this study were: 300, 350, 400, 400, 450, and 500 °C, reached with a ramp rate of 20 °C/min. All thermal treatments were carried out under a pressure of 430 mbar of argon (Ar, 5 N) for 1 h. At the end of the treatment, the samples were cooled down naturally to room temperature.

Optical transmittance and reflectance measurements were carried out with a Lambda 950 UV/Vis spectrometer (PerkinElmer). Surface and cross-section micrographs were obtained by scanning electron microscopy with an Auriga FIB-SEM microscope (Zeiss), operated at 5 kV. X-ray diffraction (XRD) patterns of GO films were recorded on an Alpha 1 (Rigaku) diffractometer using Cu-Kα (λ = 1.5406 Å) radiation, at 0.01°/s. High Resolution Transmission Electron Microscopy (HRTEM) characterization was performed using a TECNAI F20 microscope operated at 200 kV. Prior to analysis, the sample was transferred onto a lacey carbon copper grid through mechanical exfoliation. Composition profiles were studied by X-ray photoelectron spectroscopy (XPS) in the CCiTUB with a PHI 5500 multi-technique system from Physical Electronics, using a monochromatic X-ray source Al Kα line of 1486.6 eV. Raman spectra were measured using an FHR640 Horiba monochromator coupled with a CCD detector. Solid state laser (532 nm and ~70 W/cm^2 power density) was used as the excitation source. The measurements were performed in a backscattering configuration through the specific probe designed in IREC. The spectral position was corrected by imposing the main peak of the single crystalline Si to 520 cm^{-1}.

Photoelectrochemical measurements were performed using a 7 mL single-compartment cell having a 0.5 cm^2 circular window, designed at ICFO institute. 1.0 M potassium borate, BK_3O_3 (KBi) pH corrected to 9 with KOH was used as electrolyte and 0.2 M of Na_2SO_3 was added to KBi as hole scavenger in some of the experiments. Cyclic voltammetry (CV) and incident photon to current efficiency (IPCE) measurements were acquired by an SP-300 potentiostat (Biologic) scanning at 50 mV/s using a platinum wire (CH instruments CHI115) as counter electrode and an Ag/AgCl electrode in 1 M KCl (CH instruments CHI111) as reference electrode. 1-sun solar light AM 1.5G was simulated by a Sun 2000 solar simulator (Abet), incorporating a 550 W xenon lamp (Ushio), and its intensity was set to 1 sun with a calibrated silicon solar cell. IPCE measurements were carried out in the same photoelectrochemical cell setup, where samples were front illuminated with monochromatic light coming from an Oriel 260 Cornerstone monochromator (Newport

Instruments) coupled to a 300 W xenon lamp having automated extra long-pass filters to cut out more energetic second-harmonic photons from the grating. Monochromatic power intensity was recorded with a calibrated S120VC photodiode (Thorlabs). IPCE was calculated as:

$$IPCE(\%) = \frac{1.24{\cdot}10^{-3}\left(nm \times \mu W \times A^{-1}\right) \times j_{ph}(A)}{\lambda(nm) \times P_{lamp}(\mu W)} \times 100 \quad (1)$$

where j_{ph} is the photocurrent generated by the monochromatic light, λ is the wavelength and P_{lamp} is the light intensity absorbed by the sample coming from the monochromator.

3. Results and discussion

3.1. Fabrication, morphological and phase transformation characterization

SnS precursor thin films were deposited on FTO-coated glass using CBD for 1, 2, 4, and 6 h, resulting in increased FTO coverage and thicker films. A representative SEM image of the as-grown layer by 6-h CBD (Fig. 1a) shows a nanostructured surface with ~10 nm grains forming 200–400 nm close-packed agglomerates, with no FTO exposed. Cross-section SEM (Fig. 1a, inset) reveals an undulated columnar growth ranging from the FTO to the top of the agglomerates, indicating a pseudo-columnar growth.

The as-deposited layers were then annealed in a sulfur atmosphere at temperatures ranging from 300 to 500 °C for 60 min. Higher annealing temperatures degraded the FTO substrate. A significant color change is observed, from dark brown for 300 °C to yellow-brown for 500 °C (Fig. 1b). At the nanoscale, the agglomerates were still present, but the ~10 nm semi-columnar grains disappeared, and ~100 nm sheets were present, 10–20 nm thick, for the 300 °C/6 h sample (Fig. 1c). Increasing the annealing temperature (Fig. S1) resulted in highly defined hexagonal nanosheets exceeding 400 nm wide for the 500 °C/6 h sample, with thicknesses ranging from a few nanometers to ~20 nm, indicating the presence of stacked two-dimensional (2D) structures (Fig. 1d and inset). For thinner films (Figs. 1e and 500 °C/1 h), a mix of small granular structures and well-defined 2D nanosheets was present, with the latter being smaller than for thicker films. The FTO was also exposed for 1-h depositions, reducing the photoactive area. Increasing the thickness from ~100 to ~500 nm completely covers the FTO substrate (Fig. 1e and S2).

XRD (Fig. 2) diffractograms showed a clear phase change upon annealing, with the as-grown layers and those annealed at 300 and 350 °C presenting the orthorhombic α-SnS phase. The Sn_2S_3 orthorhombic phase started to appear at 350 °C and presented sharp peaks at 400 °C. Meanwhile, the SnS_2 hexagonal phase was the only one found at 450 and 500 °C, which matched the appearance of the hexagonal 2D nanosheets seen in Fig. 1d. Similar behavior is observed for thinner samples (Fig. S3a). These XRD results point at clear phase changes and minor phase intermixing, although the XRD resolution for secondary phases is limited.

The structural diversity of Sn_xS_y compounds arises primarily from tin's ability to exhibit two distinct oxidation states: Sn (II) and Sn (IV). For instance, in SnS_2, tin is in the Sn (IV) state, while in Sn_2S_3, both Sn (II) and Sn (IV) states are present. The phase relations and compositions in these compounds are heavily influenced by the S/Sn ratio and sulphuration temperature. As the S content increases, shifting the S/Sn ratio towards a higher S concentration, the total pressure required to stabilize SnS also rises. This increase in total pressure results from the need for higher partial pressure of tin to balance the elevated partial pressure of sulfur [116].

When the sulfur activity is sufficiently high, the S-rich compound Sn_2S_3 becomes stable. With even higher sulfur activity, SnS_2 can become stable as well. The chemical reactions governing the formation of these phases, as detailed in the literature [117,118], include:

$$Sn + S \rightarrow SnS \quad (2)$$

$$SnS + S \rightarrow SnS_2 \quad (3)$$

$$2SnS_2 \rightarrow Sn_2S_3 + S \quad (4)$$

$$Sn_2S_3 \rightarrow 2SnS + S \quad (5)$$

Elevated sulphuration temperatures promote the formation of SnS_2

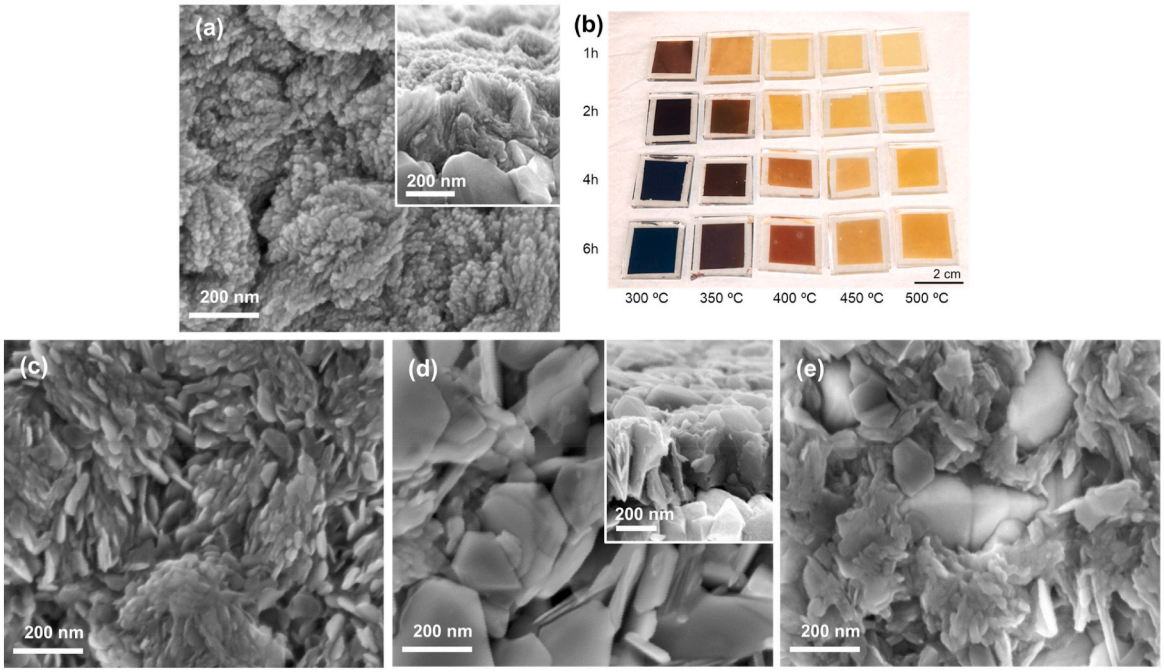

Fig. 1. a) Top view (inset: cross-section) SEM image of an as-grown 6 h CBD deposited SnS film. b) Optical photograph of the fabricated samples, with deposition times of 1–6 h and annealing temperatures of 300–500 °C. Top view (inset: cross-section) SEM image of a 6 h CBD deposited SnS film c) 300 °C and d) 500 °C annealed in sulfur atmosphere. e) SnS film deposited during 1 h and post-annealed in sulfur atmosphere at 500 °C.

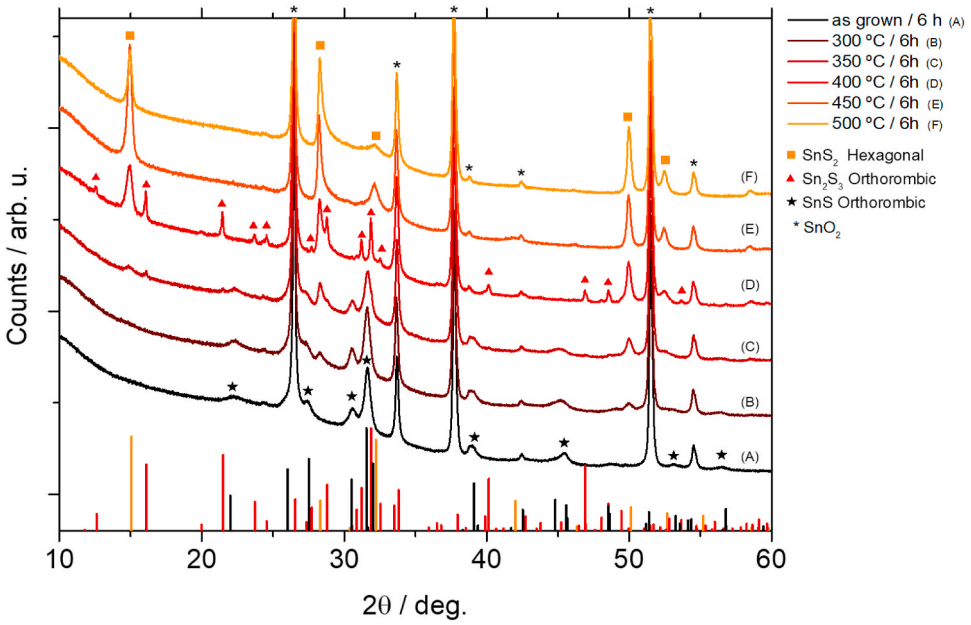

Fig. 2. XRD diffractogram of 6 h deposition SnS layers, as-grown and 300 to 500 °C annealed. XRD patters have been obtained from mindat.org: Mindat ID:1880 (SnS, Herzenbergite); Mindat ID:3042 (Sn_2S_3, Ottemannite); Mindat ID:637 (SnS_2, Berndtite).

and Sn_2S_3, leading to the near disappearance of the SnS phase as indicated by XRD analysis. At even higher temperatures, SnS and SnS_2 phases become dominant, suggesting the conversion of Sn_2S_3 back to SnS. The difference in the temperatures at which these reactions occur, compared to previous reports, may be attributed to variations in the sulphuration process. These results explain the color change and absorption profile variation of the samples upon crystallographic phase transformation, simultaneous to a valence state change from Sn^{2+} to Sn^{4+}.

XPS results (Figs. S3b–e) prove the exposed surface is composed of Sn^{4+}, with the main peak of the Sn $3d_{5/2}$ spin-orbit doublet at 486.7 eV [119], thus confirming the present crystallographic phase is SnS_2 also at the surface, together with some native oxide originating from air exposure.

The Raman scattering spectra (Fig. 3 and Fig. S4) showed that the most intense peaks in the as-deposited thin films corresponded to the α-SnS polymorph [108], with an insignificant presence of the π-SnS polymorph (peak at 107 cm^{-1}). Annealing led to the formation of the SnS_2 phase [120], with a main Raman peak at 314 cm^{-1}, and a significant reduction in the SnS phases, with their peaks disappearing for annealing temperatures ≥450 °C. Additionally, a shoulder at the red side of the main peak of SnS_2 was observed for specific annealing temperatures (350 and 400 °C), attributed to the formation of the Sn_2S_3 phase [121]. The formation of this phase was also strongly dependent on the deposition time. Nevertheless, the amount of this polymorph was low compared to the SnS_2 phase, so no significant influence is expected on further results. An increase in the deposition time also leads to the necessity of a higher annealing temperature to transform the SnS phase into SnS_2 (e.g. in Fig. 3b it is clearly seen that annealing at 400 °C results in the presence of only SnS_2 peaks in the spectra of films deposited for 1 and 2 h, and low intensity peaks of SnS and Sn_2S_3 phases can be still seen in the spectra of films deposited for 4 and 6 h).

Transmission Electron Microscopy was employed to gain insight into the microstructural configuration of the film that underwent a 6 h CBD deposition followed by annealing at 500 °C. The results are displayed in Fig. 4. The high magnification micrographs together with the Fast Fourier Transform (FFT) analysis shown in Fig. 4b and c confirm the hexagonal SnS_2 phase belonging to the space group P-3m1 (#164), in agreement with the elemental quantification obtained through Energy Dispersive X-Ray Spectroscopy shown in Fig. S5, where a 66.88 % S versus a 33.13 % Sn is measured. Fig. 4b exhibits a planar projection of SnS_2 from the c axis ([0001]), while in Fig. 4c the transversal c plane (0001) can be observed forming layered grains with thicknesses between 10 and 20 nm. This characteristic atomic stacking of the crystallites explains the quasi-planar morphology observed in the SEM micrograph shown in Fig. 1d. The presence of multiple orientations within the same flake signifies the polycrystalline nature of the structural arrangement. Additional micrographs with evidence of diverse grain orientations within the same flake can be observed in Figs. S6 and S7 tens.

3.2. Optical and photoelectrochemical characterization

The fabricated Sn_xS_y layers were tested as photoanodes for the OER reaction in 1 M KBi solution pH 9. The results show that the performance, both in generated photovoltage and photocurrent, is improved with thermal treatments at up to 500 °C in the sulfur atmosphere. The improvement is non-linear (Fig. 5a), and the thicker the absorber layer is, the more photocurrent is obtained (Figs. S8 and S9). The generated photovoltage is also observed to increase (onset voltage shift to cathodic potentials) with increasing the temperature anneal from 300 to 400 °C. Photovoltage does not increase much more when increasing to 450 or 500 °C. These non-linear increments of photocurrent and photovoltage are observed in the range of temperatures of 400–450 °C), directly related to the different optical/semiconductor properties and crystalline domains formation of the different $SnS/Sn_2S_3/SnS_2$ structures. The best performance is obtained with thermal treatments at 500 °C, where the crystalline phase changes to SnS_2 (observed by XRD, HRTEM, and Raman in Figs. 2 and 3. Slight larger hystheresis is observed for samples treated at higher temperature (Fig. 5a), in correlation with the formation of the 2D nanosheets structures observed by SEM (Fig. 1d), pointing at a capacitive effect caused by the created 2D nanoplates, having larger active area than the original columnar film, presenting some anion adsorption/desorption during cycling.

Cyclic voltammograms in dark conditions are shown in Fig. S8d, presenting small currents for all samples (lower for the samples annealed at lower temperatures, probably related to a smaller contact area with the electrolyte). Comparing the photoelectrochemical performance of the best-performing 500 °C/6 h sample with a typical NiFeOOH

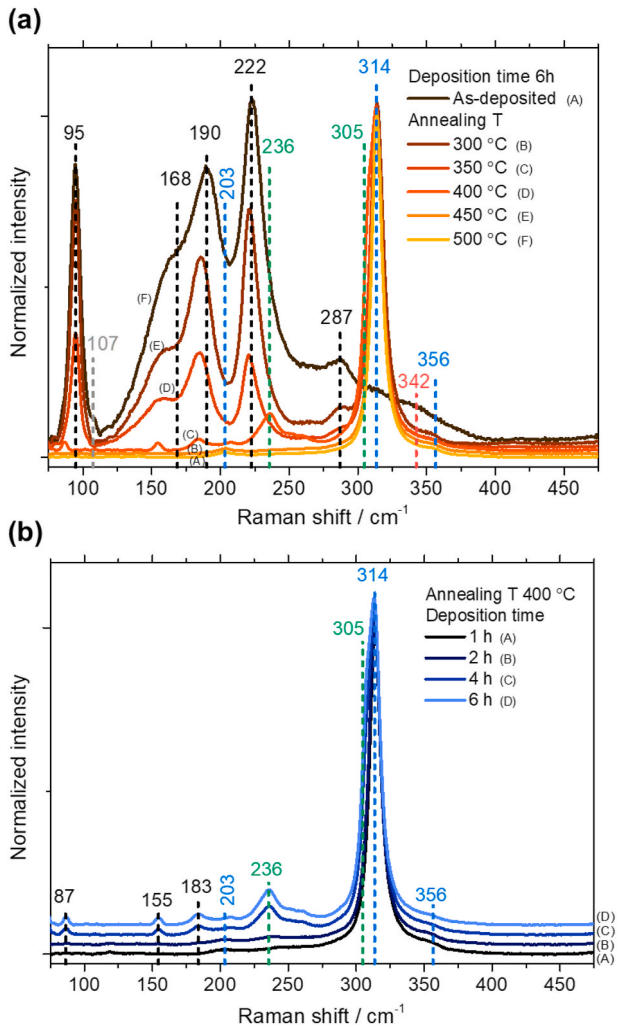

Fig. 3. Raman scattering spectra of the Sn_xS_y thin films: (a) – as deposited for 6 h and annealed at different temperatures; (b) – deposited for different times and annealed at 400 °C. The vertical dashed lines indicate the position of the main Raman peaks of different compositional polymorphs of the Sn–S system: black lines – SnS, green lines – Sn_2S_3, blue lines – SnS_2. (For interpretation of the references to color in this figure legend, the reader is referred to the Web version of this article.)

electrocatalyst photo-deposited directly on FTO and measured in the same 1 M KBi electrolyte, the photogenerated voltage by the semiconductor (cathodic shift in the onset potential for both materials) is calculated to be 1060 mV at no current (Fig. S10b). The charge separation strength, together with the ohmic drop and different surface charge transfer catalysis to OER, diminishes this voltage difference to 890 and 640 mV at 0.1 and 1 mA/cm^2, respectively. 6 h/500 °C SnS_2 was capable of standing for 10 min under 1 sun illumination before the photocurrent started to be reduced, pointing to a relative stability of this material in front of concentrated 1 M KBi pH9 electrolyte (Fig. S10).

IPCE measurements were recorded for all samples, and key information was obtained to understand the crystallographic phase change effects on photon absorption, charge generation, and transport. As observed in Fig. 5b, increasing the annealing temperature does not result in a homogeneous increase of the same IPCE plot profile. Samples annealed at 300 to 400 °C present a constant increase of the absorbed and converted light percentage, up to 65% at 325 nm, and with a drastic efficiency drop at 575 nm (2.16 eV), as observed in the inset of Fig. 5b. Meanwhile, higher thermal treatments of 450 and 500 °C result in a significant 7-fold improved conversion efficiency for wavelengths in the 500–900 nm range (down to 1.37 eV) and a special feature in the plot at 350–450 nm, showing improved photon conversion efficiency there. These drastic changes must be caused by different crystallographic phases having different band gaps and absorption/conversion/transport properties, including the reduction of defects and electronic trap states. This clearly points at SnS_2 being the one with the shortest effective and active absorption edge (Fig. 5b, inset) and also, the highest IPCE conversion (up to 75% @ 330 nm) and photocurrent generation, with no apparent voltage or catalysis loss as observed in Fig. 5a and S10a.

Similar behavior (improved performance with temperature and an effective band gap lowering at higher thermal treatments) is observed for all samples fabricated with different thicknesses, shown in Figs. S11, S12, and S13. It is worth mentioning that in Fig. S12 when zooming into the small absorption region, the role of different CBD deposited thicknesses results in a different temperature threshold change of the phase transformation and its optical absorption changes. The effective band gap lowering temperature threshold is delayed for thicker samples, as crystalline domain formation and propagation under annealing require more time and energy for thicker films. This is especially clear if we focus on the 400 °C annealed samples, which already absorb up to 900 nm when grown during 1 and 2 h, only partially for 4 h, and do not present any change in the IPCE profile in the 600–900 nm range for 6 h.

In Figs. S15–S18, the straight transmittance profiles of all samples show the same faster phase transformation for thinner samples (Fig. S15 a-d), also observed as a non-proportional to thickness absorbance profile (Fig. S16 a-e). Thus, similar trends are observed, although overlapped with the effect of scattered transmittance, which reduces the strength of transmittance analysis compared to IPCE. The specular reflectance is found to be below 20% for all samples (Fig. S17). Using the Tauc plots method, optical band gaps can only be fitted following direct-band gap equations, pointing at 0.85–1.29 eV direct band gaps for low-temperature treated samples (clearly, electrically inactive) and 2–2.4 eV direct band gaps for higher temperature treated samples (Fig. S18b), pointing at these samples being capable of converting photons below this dominating main optical band gap. This change in optical band gap is reflected as a color change of the samples from dark brown for lower band gaps, absorbing all visible spectra, to an orange-yellow color for ~2 eV band gaps, absorbing the blue-green region and thus, presenting orange-like color (Fig. 1b). The increase in optical band gap with increasing annealing temperature is in line with the cathodic shift of the onset voltage observed in Fig. 5a.

When plotting the IPCE on a logarithmic scale (Fig. S13d), even small conversion efficiency regions can be resolved. There is a change in trend with an inflection point close to ~2.2 eV, which may be attributed to an active photon-absorbing transition present in all samples. The optical thickness increases with higher treatment temperatures, resulting in different conversion efficiency. All samples present the same slope for low energetic wavelengths but with a different vertical axis position. This may be due to a superficial nanometric SnS_2 layer that is too thin to be detected by crystallographic analysis techniques. The same experimental conditions were applied to a $BiVO_4$ photoanode (Fig. S14), which did not show any response in this 550–900 nm range, thus ruling out any experimental artifact signal. On the other hand, the 500 °C/6 h sample studied herein presents two main inflection points in IPCE logarithmic plots at 2.42 and 2.13 eV, indicating the possibility of SnS_2 having both direct and indirect band gap transitions, maybe related to the reported anisotropic absorption coefficient [89,122,123] for SnS_2 and the hexagonal structures crystallographic orientations observed by HRTEM (Fig. 4c) or to electronic confinement properties of the low-dimensional 2D nanosheets reducing the effective band gap and improving charge extraction and transport properties [68,73,74], allowing photon absorption down to 900 nm.

This work postulates that Sn_xS_y materials have the potential for use in photoelectrochemical water splitting, with SnS_2 providing 1.6 mA/cm^2 at 1.23 V_{RHE} and >75% IPCE conversions as reported in this study. These results highlight the importance of facile methods such as chemical bath deposition for the fabrication of earth-abundant sulfides.

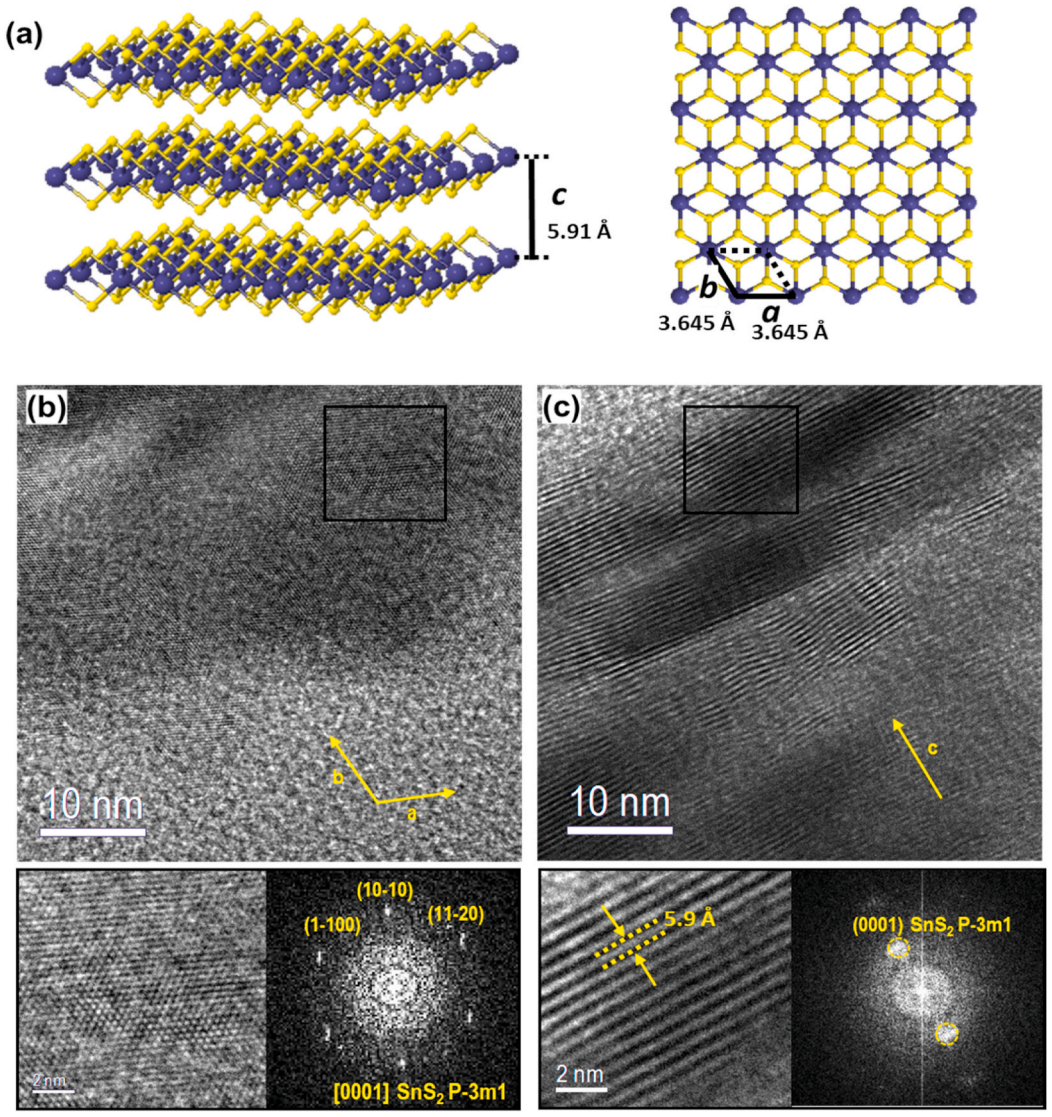

Fig. 4. HRTEM analyses of the microstructure of the 6 h CBD deposited film annealed at 500 °C. (a) 3D atomic model of the SnS_2 phase belonging to space group 164 P-3m1 and projection of the crystal arrangement along the c-axis. (b), (c) HRTEM micrographs from different areas of the same flake evidencing a polycrystalline nature of the structure with observable nanograins displaying different orientations. A planar view from [0001] SnS_2 zone axis is observed in (b) and a transversal view with visible c plane (SnS_2(0001)) is observable in (c).

4. Conclusions

The results of this study demonstrate the potential of SnS_2 materials for photoelectrochemical water splitting. Utilizing a facile CBD method for the fabrication of Sn_xS_y photoanodes yielded nanocrystalline SnS layers presenting a dark brown color and an undulated columnar pseudo-epitaxial structure up to 300 nm thick. Subsequent thermal sulfurization led to the formation of polycrystalline SnS_2 samples, featuring multilayer 2D hexagonal nanosheets exceeding 400 nm in width at the 500 °C annealing temperature.

These samples exhibited commendable performances, including photogenerated voltages of 1.06 V, photocurrents surpassing 1.6 mA/cm^2 @ 1.23V_{RHE}, IPCE conversion efficiencies of 75% at 330 nm wavelengths, and an OER-favorable catalytic surface. Analysis of the data by Raman, HRTEM, XRD, and optoelectronic means revealed a crystalline phase transition from orthorhombic α-SnS to Sn_2S_3, followed by the formation of hexagonal SnS_2. The intermediate Sn_2S_3 phase is not often reported, while the hexagonal SnS_2 phase exhibited the smallest electronically active band gap, resulting in superior visible-light conversion and overall performance.

IPCE characterization highlighted the photon conversion capabilities of SnS_2 in the 500–900 nm range (down to 1.37 eV), with a maximum IPCE conversion of 75% at 330 nm. The observed IPCE profile indicates that CBD-grown SnS_2 2D nanosheet photoanodes manifest significant potential for enhancing absorption and conversion across the entire visible light spectrum, positioning them as promising materials for efficient solar hydrogen production.

Associated content

Supporting Information. Sample photos, UV–Vis transmittance and reflectance spectra, Tauc plots, SEM images, XRD, HRTEM, Raman, cyclic voltammetries, and IPCE supporting images are supplied in an additional document.

CRediT authorship contribution statement

Yudania Sánchez: Writing – review & editing, Writing – original draft, Investigation, Data curation, Conceptualization. **Maxim Guc:** Validation, Methodology, Formal analysis, Data curation. **Sara Martí-**

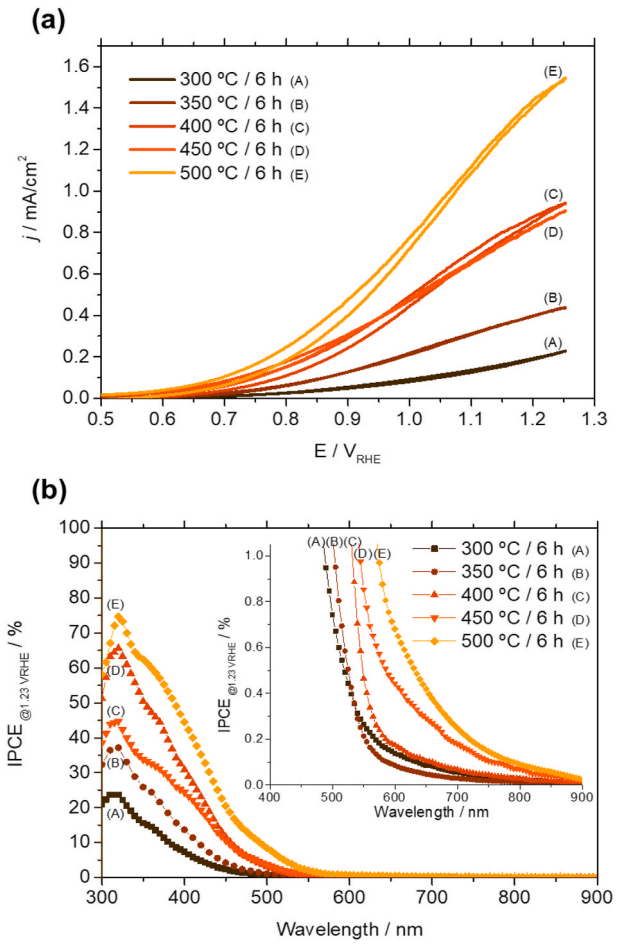

Fig. 5. a) Cyclic voltammetries of samples fabricated by 6 h CBD process thermally treated at temperatures from 300 to 500 °C in sulfur atmosphere and measured in 1 M KBi pH 9 electrolytes and 1 sun AM 1.5G solar illumination. b) IPCE measurements of samples fabricated by 6 h CBD process thermally treated at temperatures from 300 to 500 °C in the sulfur atmosphere measured in 1 M KBi pH 9 electrolytes and exposed to monochromatic illumination.

Sánchez: Writing – original draft, Validation, Investigation, Formal analysis, Data curation. **Maykel Jiménez-Guerra:** Methodology, Investigation, Data curation. **Shadai Lugo-Loredo:** Writing – review & editing, Writing – original draft, Validation, Supervision, Resources, Project administration, Investigation, Funding acquisition, Formal analysis, Data curation. **Jordi Arbiol:** Writing – review & editing, Writing – original draft, Visualization, Supervision, Software, Resources, Project administration, Methodology, Investigation, Funding acquisition, Formal analysis, Data curation. **Alejandro Perez-Rodriguez:** Resources, Project administration, Funding acquisition. **Jordi Martorell:** Writing – review & editing, Validation, Supervision, Resources, Project administration, Funding acquisition. **Carles Ros:** Writing – review & editing, Writing – original draft, Visualization, Validation, Supervision, Software, Resources, Project administration, Methodology, Investigation, Formal analysis, Data curation, Conceptualization.

Declaration of competing interest

The authors declare the following financial interests/personal relationships which may be considered as potential competing interests: Jordi Martorell reports financial support was provided by Horizon Europe. Jordi Martorell reports financial support was provided by Spain Ministry of Science and Innovation. Jordi Martorell reports financial support was provided by Cellex Foundation. Jordi Martorell reports financial support was provided by Mir-Puig Private Foundation. Jordi Martorell reports financial support was provided by Generalitat de Catalunya Ministry of Research and Universities. Carles Ros reports financial support was provided by Spain Ministry of Science and Innovation. Jordi Martorell reports financial support was provided by Barcelona Institute of Science and Technology. Alejandro Perez-Rodriguez reports financial support was provided by Generalitat de Catalunya Ministry of Research and Universities. Maxim Guc reports financial support was provided by Spain Ministry of Science and Innovation. Jordi Arbiol reports financial support was provided by Spain Ministry of Science and Innovation. Jordi Arbiol reports financial support was provided by Generalitat de Catalunya Ministry of Research and Universities. If there are other authors, they declare that they have no known competing financial interests or personal relationships that could have appeared to influence the work reported in this paper.

Acknowledgment

ICFO acknowledge financial support from LICROX and SOREC2 EU-Funded projects (Codes: 951843 and 101084326), the BIST Program and Severo Ochoa Program. This work was partially funded by CEX2019-000910-S (MCIN/AEI/10.13039/501100011033 and PID2020-112650RB-I00), Fundació Cellex, Fundació Mir-Puig, and Generalitat de Catalunya through CERCA. C.R. acknowledges support from the MCIN/AEI JdC-F Fellowship (FJC2020-043223-I) and the Severo Ochoa Excellence Post-doctoral Fellowship (CEX2019-000910-S). Authors from IREC belong to the MNT-Solar Consolidated Research Group of the "Generalitat de Catalunya" (ref. 2021 SGR 01286) and are grateful to European Regional Development Funds (ERDF, FEDER Programa Competitivitat de Catalunya 2007–2013). M.G. acknowledges the financial support from Spanish Ministry of Science, Innovation and Universities within the Juan de la Cierva fellowship (IJC2018-038199-I). ICN2 acknowledges funding from Generalitat de Catalunya 2021SGR00457. The authors thank support from the project NANOGEN (PID2020-116093RB-C43), funded by MCIN/AEI/10.13039/501100011033/and by "ERDF A way of making Europe", by the "European Union". ICN2 is supported by the Severo Ochoa program from Spanish MCIN/AEI (Grant No.: CEX2021-001214-S) and is funded by the CERCA Programme/Generalitat de Catalunya.

Appendix A. Supplementary data

Supplementary data to this article can be found online at https://doi.org/10.1016/j.ijhydene.2024.06.160.

References

[1] Jiang C, Moniz SJA, Wang A, Zhang T, Tang J. Photoelectrochemical devices for solar water splitting - materials and challenges. Chem Soc Rev 2017;46:4645–60. https://doi.org/10.1039/C6CS00306K.
[2] Moss B, Babacan O, Kafizas A, Hankin A. A review of inorganic photoelectrode developments and reactor scale-up challenges for solar hydrogen production. Adv Energy Mater 2021;2003286:1–43. https://doi.org/10.1002/aenm.202003286.
[3] Ros C, Andreu T, Morante JR. Photoelectrochemical water splitting: a road from stable metal oxides to protected thin film solar cells. J Mater Chem A Mater 2020: 10625–69. https://doi.org/10.1039/d0ta02755c.
[4] Sivula K, Prevot MS. Photoelectrochemical tandem cells for solar water splitting. J Phys Chem C 2013;117:17879–93. https://doi.org/10.1021/jp405291g.
[5] Mei B, Pedersen T, Malacrida P, Bae D, Frydendal R, Hansen O, Vesborg PCK, Seger B, Chorkendorff I. Crystalline TiO 2 : a generic and effective electron-conducting protection layer for photoanodes and -cathodes. J Phys Chem C 2015; 119:15019–27. https://doi.org/10.1021/acs.jpcc.5b04407.
[6] Ros C, Andreu T, Hernández-Alonso MD, Penelas-Pérez G, Arbiol J, Morante JR. Charge transfer characterization of ALD-grown TiO2 protective layers in silicon photocathodes. ACS Appl Mater Interfaces 2017;9:17932–41. https://doi.org/10.1021/acsami.7b02996.
[7] Ros C, Carretero NM, David J, Arbiol J, Andreu T, Morante JR. Insight into the degradation mechanisms of atomic layer deposited TiO2 as photoanode protective layer. ACS Appl Mater Interfaces 2019;11:29725–35. https://doi.org/10.1021/acsami.9b05724.
[8] Bae D, Pedersen T, Seger B, Malizia M, Kuznetsov A, Hansen O, Chorkendorff I, Vesborg PCK. Back-illuminated Si photocathode: a combined experimental and

theoretical study for photocatalytic hydrogen evolution. Energy Environ Sci 2015;8:650–60. https://doi.org/10.1039/C4EE03723E.
[9] McKone JR, Warren EL, Bierman MJ, Boettcher SW, Brunschwig BS, Lewis NS, Gray HB. Evaluation of Pt, Ni, and Ni–Mo electrocatalysts for hydrogen evolution on crystalline Si electrodes. Energy Environ Sci 2011;4:3573–83. https://doi.org/10.1039/c1ee01488a.
[10] Hu S, Shaner MR, a Beardslee J, Lichterman M, Brunschwig BS, Lewis NS. Amorphous TiO_2 coatings stabilize Si, GaAs, and GaP photoanodes for efficient water oxidation. Science 2014;344:1005–9. https://doi.org/10.1126/science.1251428.
[11] Yang F, Nielander AC, Grimm RL, Lewis NS. Photoelectrochemical behavior of n-type GaAs(100) electrodes coated by a single layer of graphene. J Phys Chem C 2016;120:6989–95. https://doi.org/10.1021/acs.jpcc.6b00232.
[12] Kraft A, Görig B, Heckner KH. ITO coated n-GaAs electrodes for photoelectrochemical solar cells. Sol Energy Mater Sol Cell 1994;32:151–8. https://doi.org/10.1016/0927-0248(94)90300-X.
[13] Ros C, Andreu T, Giraldo S, Sánchez Y, Morante JR. Conformal chalcopyrite based photocathode for solar refinery applications. Sol Energy Mater Sol Cell 2016;158:184–8. https://doi.org/10.1016/j.solmat.2016.01.031.
[14] Guijarro N, Prévot MS, Yu X, Jeanbourquin XA, Bornoz P, Bourée W, Johnson M, Le Formal F, Sivula K. A bottom-up approach toward all-solution-processed high-efficiency Cu(in,Ga)S 2 photocathodes for solar water splitting. Adv Energy Mater 2016:n/a. https://doi.org/10.1002/aenm.201501949. n/a.
[15] Yokoyama D, Minegishi T, Maeda K, Katayama M, Kubota J, Yamada A, Konagai M, Domen K. Photoelectrochemical water splitting using a Cu(In,Ga)Se2 thin film. Electrochem Commun 2010;12:851–3. https://doi.org/10.1016/j.elecom.2010.04.004.
[16] Jacobsson TJ. Highly efficient CIGS based devices for solar hydrogen production and size dependent properties of ZnO quantum dots. 2014.
[17] Jacobsson TJ, Fjallstrom V, Sahlberg M, Edoff M, Edvinsson T. A monolithic device for solar water splitting based on series interconnected thin film absorbers reaching over 10% solar-to-hydrogen efficiency. Energy Environ Sci 2013;6:3676–83. https://doi.org/10.1039/C3ee42519c.
[18] Ros C, Andreu T, Giraldo S, Izquierdo-Roca V, Saucedo E, Morante JR. Turning earth abundant kesterite-based solar cells into efficient protected water splitting photocathodes. ACS Appl Mater Interfaces 2018;10:13425–33. https://doi.org/10.1021/acsami.8b00062.
[19] Arai T, Tajima S, Sato S, Uemura K, Morikawa T, Kajino T. Selective CO2 conversion to formate in water using a CZTS photocathode modified with a ruthenium complex polymer. Chem Commun 2011;47:12664. https://doi.org/10.1039/c1cc16160a.
[20] Guan Z, Luo W, Zou Z. Formation mechanism of ZnS impurities and their effect on photoelectrochemical properties on a Cu2ZnSnS4 photocathode. CrystEngComm 2014:2929–36. https://doi.org/10.1039/c3ce42373e.
[21] Shao PW, Li CT, Ho KC, Cheng KW. Catalytic and photoelectrochemical performances of Cu-Zn-Sn-Se thin films prepared using selenization of electrodeposited Cu-Zn-Sn metal precursors. J Power Sources 2015;286:47–57. https://doi.org/10.1016/j.jpowsour.2015.03.101.
[22] Sivula K. Enhancing the charge separation in nanocrystalline Cu 2 ZnSnS 4 photocathodes for photoelectrochemical application: the role of surface modi fi cations. J Phys Chem Lett 2014;5:3902–8. https://doi.org/10.1021/jz501996s.
[23] Li B-J, Yin P-F, Zhou Y-Z, Gao Z-M, Ling T, Du X-W. Single crystalline Cu\n2\n ZnSnS\n 4\n nanosheet arrays for efficient photochemical hydrogen generation. RSC Adv 2015;5:2543–9. https://doi.org/10.1039/C4RA13721C.
[24] JiangGunawan F, Harada T, Kuang Y, Minegishi T, Domen K, Ikeda S. Pt/In2S3/CdS/Cu2ZnSnS4 thin film as an efficient and stable photocathode for water reduction under sunlight radiation. J Am Chem Soc 2015;137:13691–7. https://doi.org/10.1021/jacs.5b09015.
[25] Koo B, Nam SW, Haight R, Kim S, Oh S, Cho M, Oh J, Lee JY, Ahn BT, Shin B. Tailoring photoelectrochemical performance and stability of Cu(in,Ga)Se2 photocathode via TiO2-coupled buffer layers. ACS Appl Mater Interfaces 2017;9:5279–87. https://doi.org/10.1021/acsami.6b15168.
[26] Seger B, Tilley DS, Pedersen T, Vesborg PCKK, Hansen O, Grätzel M, Chorkendorff I. Silicon protected with atomic layer deposited TiO2: durability studies of photocathodic H2 evolution. RSC Adv 2013;3:25902–7. https://doi.org/10.1039/c3ra45966g.
[27] Seger B, Tilley SD, Pedersen T, Vesborg PCKK, Hansen O, Grätzel M, Chorkendorff I, Graetzel M, Chorkendorff I. Silicon protected with atomic layer deposited TiO2: conducting versus tunnelling through TiO2. J Mater Chem A Mater 2013;1:15089–94. https://doi.org/10.1039/c3ta12309j.
[28] Mei B, Pedersen T, Malacrida P, Bae D, Frydendal R, Hansen O, Vesborg PCKK, Seger B, Chorkendorff I. Crystalline TiO 2 : a generic and effective electron-conducting protection layer for photoanodes and -cathodes. J Phys Chem C 2015;119:15019–27. https://doi.org/10.1021/acs.jpcc.5b04407.
[29] Chihi A, Boujmil MF, Bessais B. Investigation on the performance of CIGS/TiO2 heterojunction using SCAPS software for highly efficient solar cells. J Electron Mater 2017;46:5270–7. https://doi.org/10.1007/s11664-017-5547-0.
[30] Zhao J, Minegishi T, Zhang L, Zhong M, Gunawan G, Nakabayashi M, Ma G, Hisatomi T, Katayama M, Ikeda S, Shibata N, Yamada T, Domen K. Enhancement of solar hydrogen evolution from water by surface modification with CdS and TiO2on porous CuInS2 photocathodes prepared by an electrodeposition-sulfurization method. Angew Chem Int Ed 2014;53:11808–12. https://doi.org/10.1002/anie.201406483.
[31] Scheuermann AG, Kemp KW, Tang K, Lu DQ, Satterthwaite PF, Ito T, Chidsey CEDD, McIntyre PC, Mc Intyre PC. Conductance and capacitance of bilayer protective oxides for silicon water splitting anodes. Energy Environ Sci 2016;9:1–26. https://doi.org/10.1039/C5EE02484F.
[32] Scheuermann AG, Lawrence JP, Meng AC, Tang K, Hendricks OL, Chidsey CED, McIntyre PC. Titanium oxide crystallization and interface defect passivation for high performance insulator-protected Schottky junction MIS photoanodes. ACS Appl Mater Interfaces 2016;8:14596–603. https://doi.org/10.1021/acsami.6b03688.
[33] Scheuermann AG, Prange JD, Gunji M, Chidsey CED, McIntyre PC. Effects of catalyst material and atomic layer deposited TiO2oxide thickness on the water oxidation performance of metal-insulator-silicon anodes. Energy Environ Sci 2013;6:2487–96. https://doi.org/10.1039/c3ee41178h.
[34] Azarpira A, Lublow M, Steigert A, Bogdanoff P, Greiner D, Kaufmann CA, Krüger M, Gernert U, Van De Krol R, Fischer A, Schedel-Niedrig T. Efficient and stable TiO2:Pt-Cu(in,Ga)Se2 composite photoelectrodes for visible light driven hydrogen evolution. Adv Energy Mater 2015;5:1–9. https://doi.org/10.1002/aenm.201402148.
[35] Wick R, Tilley SD. Photovoltaic and photoelectrochemical solar energy conversion with Cu2O. J Phys Chem C 2015;119:26243–57. https://doi.org/10.1021/acs.jpcc.5b08397.
[36] Flox C, Murcia-López S, Carretero NM, Ros C, Morante JR, Andreu T. Role of bismuth in the electrokinetics of silicon photocathodes for solar rechargeable vanadium redox flow batteries. ChemSusChem 2018;11:125–9. https://doi.org/10.1002/cssc.201701879.
[37] Imran H, Abdolkader TM, Butt NZ. Carrier-selective NiO/Si and TiO2/Si contacts for silicon heterojunction solar cells. IEEE Trans Electron Dev 2016;63:3584–90. https://doi.org/10.1109/TED.2016.2585523.
[38] Ros C, Andreu T, David JJ, Arbiol J, Morante JRJR. Degradation and regeneration mechanisms of NiO protective layers deposited by ALD on photoanodes. J Mater Chem A Mater 2019;7:21892–902. https://doi.org/10.1039/c9ta08638b.
[39] Han T, Shi Y, Song X, Mio A, Valenti L, Hui F, Privitera S, Lombardo S, Lanza M. Ageing mechanisms of highly active and stable nickel-coated silicon photoanodes for water splitting. J Mater Chem A 2016;4:8053–60. https://doi.org/10.1039/C5TA09990K.
[40] Sun K, Kuang Y, Verlage E, Brunschwig BS, Tu CW, Lewis NS. Sputtered NiOx films for stabilization of p+n-InP photoanodes for solar-driven water oxidation. Adv Energy Mater 2015;5:1–8. https://doi.org/10.1002/aenm.201402276.
[41] Laskowski FAL, Nellist MR, Venkatkarthick R, Boettcher SW. Junction behavior of n-Si photoanodes protected by thin Ni elucidated from dual working electrode photoelectrochemistry. Energy Environ Sci 2017;10:570–9. https://doi.org/10.1039/c6ee03505a.
[42] Turner JA. A nickel finish protects silicon photoanodes for water splitting. Science 1979;342:2. https://doi.org/10.1126/science.1246766. 2013.
[43] Ros C, Murcia-López S, Garcia X, Rosado M, Arbiol J, Llorca J, Morante JR. Facing seawater splitting challenges by regeneration with Ni−Mo−Fe bifunctional electrocatalyst for hydrogen and oxygen evolution. ChemSusChem 2021:1–11. https://doi.org/10.1002/cssc.202100194.
[44] Liu Z, Li C, Xiao Y, Wang F, Yu Q, Faheem MB, Zhou T, Li Y. Tailored NiFe catalyst on silicon photoanode for efficient photoelectrochemical water oxidation. J Phys Chem C 2020;124:2844–50. https://doi.org/10.1021/acs.jpcc.9b10967.
[45] Li F, Li Y, Zhuo Q, Zhou D, Zhao Y, Zhao Z, Wu X, Shan Y, Sun L. Electroless plating NiFeP alloy on the surface of silicon photoanode for efficient photoelectrochemical water oxidation. ACS Appl Mater Interfaces 2020. https://doi.org/10.1021/acsami.9b19418.
[46] Ahmet IY, Ma Y, Jang JW, Henschel T, Stannowski B, Lopes T, Vilanova A, Mendes A, Abdi FF, Van De Krol R. Demonstration of a 50 cm2 BiVO4 tandem photoelectrochemical-photovoltaic water splitting device. Sustain Energy Fuels 2019;3:2366–79. https://doi.org/10.1039/c9se00246d.
[47] Wang S, Chen P, Bai Y, Yun JH, Liu G, Wang L. New BiVO4 dual photoanodes with enriched oxygen vacancies for efficient solar-driven water splitting. Adv Mater 2018;30:1–7. https://doi.org/10.1002/adma.201800486.
[48] Kim JH, Jo Y, Kim JH, Jang JW, Kang HJ, Lee YH, Kim DS, Jun Y, Lee JS. Wireless solar water splitting device with robust cobalt-catalyzed, dual-doped BiVO4 photoanode and perovskite solar cell in tandem: a dual absorber artificial leaf. ACS Nano 2015;9:11820–9. https://doi.org/10.1021/acsnano.5b03859.
[49] Xue D, Kan M, Qian X, Zhao Y. A tandem water splitting cell based on nanoporous BiVO4 photoanode cocatalyzed by ultrasmall cobalt borate sandwiched with conformal TiO2 layers. ACS Sustainable Chem Eng 2018;6:16228–34. https://doi.org/10.1021/acssuschemeng.8b03078.
[50] Fujishima A, Honda K. Electrochemical photolysis of water at a semiconductor electrode. Nature 1972;238:37–8. https://doi.org/10.1038/238037a0.
[51] Ros C, Fabrega C, Monllor-Satoca D, Hernández-Alonso MD, Penelas-Pérez G, Morante JR, Andreu T. Hydrogenation and structuration of TiO 2 nanorods photoanodes: doping level and the effect of illumination in trap-states filling. J Phys Chem C 2018;122:3295–304. https://doi.org/10.1021/acs.jpcc.7b12468.
[52] Tang P, Xie H, Ros C, Han L, Biset-Peiró M, He Y, Kramer W, Rodríguez AP, Saucedo E, Galán-Mascarós JR, Andreu T, Morante JR, Arbiol J. Enhanced photoelectrochemical water splitting of hematite multilayer nanowire photoanodes by tuning the surface state via bottom-up interfacial engineering. Energy Environ Sci 2017;10:2124–36. https://doi.org/10.1039/c7ee01475a.
[53] Klahr B, Gimenez S, Fabregat-Santiago F, Bisquert J, Hamann TW. Electrochemical and photoelectrochemical investigation of water oxidation with hematite electrodes. Energy Environ Sci 2012;5:7626. https://doi.org/10.1039/c2ee21414h.
[54] Zhong DK, Cornuz M, Sivula K, Grätzel M, Gamelin DR. Photo-assisted electrodeposition of cobalt-phosphate (Co-Pi) catalyst on hematite photoanodes

for solar water oxidation. Energy Environ Sci 2011;4:1759–64. https://doi.org/10.1039/c1ee01034d.
[55] Zhao Y, Westerik P, Santbergen R, Zoethout E, Gardeniers H, Bieberle-Hütter A. From geometry to activity: a quantitative analysis of WO3/Si micropillar arrays for photoelectrochemical water splitting. Adv Funct Mater 2020;1909157:1–10. https://doi.org/10.1002/adfm.201909157.
[56] Fàbrega C, Murcia-López S, Monllor-Satoca D, Prades JD, Hernández-Alonso MD, Penelas G, Morante JR, Andreu T. Efficient WO3 photoanodes fabricated by pulsed laser deposition for photoelectrochemical water splitting with high faradaic efficiency. Appl Catal, B 2016;189:133–40. https://doi.org/10.1016/j.apcatb.2016.02.047.
[57] Chen L, Toma FM, Cooper JK, Lyon A, Lin Y, Sharp ID, Ager JW. Mo-doped BiVO4 photoanodes synthesized by reactive sputtering. ChemSusChem 2015;8:1066–71. https://doi.org/10.1002/cssc.201402984.
[58] Geronimo L, Ferreira CG, Gacha V, Raptis D, Martorell J, Ros C. Understanding the internal conversion efficiency of BiVO 4/SnO 2 photoanodes for solar water splitting: an experimental and computational analysis. ACS Appl Energy Mater 2024. https://doi.org/10.1021/acsaem.3c02775.
[59] Ferreira CG, Sansierra C, Bernal-Texca F, Zhang M, Ros C, Martorell J. Bias-free solar-to-hydrogen conversion in a BiVO 4/PM6:Y6 compact tandem with optically balanced light absorption. Energy Environ Mater 2023:1–8. https://doi.org/10.1002/eem2.12679.
[60] Kim TW, Ping Y, Galli GA, Choi KS. Simultaneous enhancements in photon absorption and charge transport of bismuth vanadate photoanodes for solar water splitting. Nat Commun 2015;6:1–10. https://doi.org/10.1038/ncomms9769.
[61] Kuang Y, Jia Q, Nishiyama H, Yamada T, Kudo A, Domen K. A front-illuminated nanostructured transparent BiVO4 photoanode for >2% efficient water splitting. Adv Energy Mater 2016;6:2–8. https://doi.org/10.1002/aenm.201501645.
[62] Han HS, Shin S, Kim DH, Park IJ, Kim JS, Huang PS, Lee JK, Cho IS, Zheng X. Boosting the solar water oxidation performance of a BiVO4 photoanode by crystallographic orientation control. Energy Environ Sci 2018;11:1299–306. https://doi.org/10.1039/c8ee00125a.
[63] Gao J, Li J, Liu Y, Xia M, Finfrock YZ, Zakeeruddin SM, Ren D, Grätzel M. Solar reduction of carbon dioxide on copper- tin electrocatalysts with energy conversion ef fi ciency near 20. https://doi.org/10.1038/s41467-022-33049-7; 2022.
[64] Geronimo L, Ferreira CG, Gacha V, Raptis D, Martorell J, Ros C. Understanding the internal conversion efficiency of BiVO4/SnO2 photoanodes for solar water splitting: an experimental and computational analysis. ACS Appl Energy Mater 2024. https://doi.org/10.1021/acsaem.3c02775.
[65] Jacobsson TJ. Photoelectrochemical water splitting: an idea heading towards obsolescence? Energy Environ Sci 2018;11:1977–9. https://doi.org/10.1039/c8ee00772a.
[66] Montoya JH, Seitz LC, Chakthranont P, Vojvodic A, Jaramillo TF, Nørskov JK. Materials for solar fuels and chemicals. Nat Mater 2016;16:70–81. https://doi.org/10.1038/nmat4778.
[67] S. Hadke, M. Huang, C. Chen, Y.F. Tay, S. Chen, J. Tang, L. Wong, Emerging Chalcogenide Thin Films for Solar Energy Harvesting Devices, (n.d.). https://doi.org/10.1021/acs.chemrev.1c00301.
[68] Zhang F, Pei J, Baev A, Samoc M, Ge Y, Prasad PN, Zhang H. Photo-dynamics in 2D materials: processes, tunability and device applications. Phys Rep 2022;993:1–70. https://doi.org/10.1016/j.physrep.2022.09.005.
[69] Patel M, Kumar M, Kim J, Kim YK. Photocurrent enhancement by a rapid thermal treatment of nanodisk-shaped SnS photocathodes. J Phys Chem Lett 2017;8:6099–105. https://doi.org/10.1021/acs.jpclett.7b02998.
[70] Y.S. Choudhary, L. Jothi, G. Nageswaran, Electrochemical Characterization of p-Type Semiconducting Tungsten Disulfide Photocathodes: Efficient Photoreduction Processes at Semiconductor/Liquid Electrolyte Interfaces, J Am Chem Soc 105 (n.d.) 2246–2256. https://doi.org/10.1016/B978-0-323-46140-5.00002-9.
[71] Hasani A, Van Le Q, Tekalgne M, Choi MJ, Choi S, Lee TH, Kim H, Ahn SH, Jang HW, Kim SY. Fabrication of a WS2/p-Si heterostructure photocathode using direct hybrid thermolysis. ACS Appl Mater Interfaces 2019;11:29910–6. https://doi.org/10.1021/acsami.9b08654.
[72] Yang W, Zhang X, Tilley SD. Emerging binary chalcogenide light absorbers: material specific promises and challenges. Chem Mater 2021;33:3467–89. https://doi.org/10.1021/acs.chemmater.1c00741.
[73] Chernikov A, Ruppert C, Hill HM, Rigosi AF, Heinz TF. Population inversion and giant bandgap renormalization in atomically thin WS 2 layers. Nat Photonics 2015;9:466–70. https://doi.org/10.1038/nphoton.2015.104.
[74] Maserati L, Prato M, Pecorario S, Passarella B, Perinot A, Thomas AA, Melloni F, Natali D, Caironi M. Photo-electrical properties of 2D quantum confined metal-organic chalcogenide nanocrystal films. Nanoscale 2021;13:233–41. https://doi.org/10.1039/d0nr07409h.
[75] Wang S, Wang L. Recent progress of tungsten- and molybdenum-based semiconductor materials for solar-hydrogen production. Tungsten 2019;1:19–45. https://doi.org/10.1007/s42864-019-00006-9.
[76] McKone JR, Pieterick AP, Gray HB, Lewis NS. Hydrogen evolution from Pt/Ru-coated p-type WSe2 photocathodes. J Am Chem Soc 2013;135:223–31. https://doi.org/10.1021/ja308581g.
[77] Mckone JR, Pieterick AP, Gray HB, Lewis NS. Supporting information : hydrogen evolution from Pt/Ru-coated p-type WSe2 photocathodes. J Am Chem Soc 2013;135.
[78] Velický M, Bissett MA, Woods CR, Toth PS, Georgiou T, Kinloch IA, Novoselov KS, Dryfe RAW. Photoelectrochemistry of pristine mono- and few-layer MoS2. Nano Lett 2016;16:2023–32. https://doi.org/10.1021/acs.nanolett.5b05317.
[79] Xu X, Hu J, Yin Z, Xu C. Photoanode current of large-area MoS2 ultrathin nanosheets with vertically mesh-shaped structure on indium tin oxide. ACS Appl Mater Interfaces 2014:5983–7. https://doi.org/10.1021/am501159s.
[80] Yu X, Sivula K. Layered 2D semiconducting transition metal dichalcogenides for solar energy conversion. Curr Opin Electrochem 2017:1–7. https://doi.org/10.1016/j.coelec.2017.03.007.
[81] Zhou J, Dai S, Dong W, Su X, Fang L, Zheng F, Wang X, Shen M. Efficient and stable MoS2 catalyst integrated on Si photocathodes by photoreduction and post-annealing for water splitting. Appl Phys Lett 2016;108:213905. https://doi.org/10.1063/1.4952739.
[82] Zuo Y, Liu Y, Li J, Du R, Yu X, Xing C, Zhang T, Yao L, Arbiol J, Llorca J, Sivula K, Guijarro N, Cabot A. Solution-processed ultrathin SnS 2 -Pt nanoplates for photoelectrochemical water oxidation. ACS Appl Mater Interfaces 2019;11:6918–26. https://doi.org/10.1021/acsami.8b17622.
[83] Mohamed Abouelela M, Kawamura G, Matsuda A. Metal chalcogenide-based photoelectrodes for photoelectrochemical water splitting. J Energy Chem 2022;73:189–213. https://doi.org/10.1016/j.jechem.2022.05.022.
[84] Wang H, Xia Y, Li H, Wang X, Yu Y, Jiao X, Chen D. Highly active deficient ternary sulfide photoanode for photoelectrochemical water splitting. Nat Commun 2020;11:1–11. https://doi.org/10.1038/s41467-020-16800-w.
[85] Zhang Y, Seghete D, Abdulagatov A, Gibbs Z, Cavanagh A, Yang R, George S, Lee YC. Investigation of the defect density in ultra-thin Al2O3 films grown using atomic layer deposition. Surf Coat Technol 2011;205:3334–9. https://doi.org/10.1016/j.surfcoat.2010.12.001.
[86] Lin Y, Battaglia C, Boccard M, Hettick M, Yu Z, Ballif C, Ager JW, Javey A. Amorphous Si thin film based photocathodes with high photovoltage for efficient hydrogen production. Nano Lett 2013;13:5615–8. https://doi.org/10.1021/nl403265k.
[87] Poli I, Hintermair U, Regue M, Kumar S, Sackville EV, Baker J, Watson TM, Eslava S, Cameron PJ. Graphite-protected CsPbBr3 perovskite photoanodes functionalised with water oxidation catalyst for oxygen evolution in water. Nat Commun 2019;10:1–10. https://doi.org/10.1038/s41467-019-10124-0.
[88] Ma G, Minegishi T, Yokoyama D, Kubota J, Domen K. Photoelectrochemical hydrogen production on Cu2ZnSnS 4/Mo-mesh thin-film electrodes prepared by electroplating. Chem Phys Lett 2011;501:619–22. https://doi.org/10.1016/j.cplett.2010.11.081.
[89] Zandalazini CI, Navarro Sanchez J, Albanesi EA, Gupta Y, Arun P. Contribution of lattice parameter and vacancies on anisotropic optical properties of tin sulphide. J Alloys Compd 2018;746:9–18. https://doi.org/10.1016/j.jallcom.2018.02.262.
[90] Kim JH, Kaneko H, Minegishi T, Kubota J, Domen K, Lee JS. Overall photoelectrochemical water splitting using tandem cell under simulated sunlight. ChemSusChem 2016;9:61–6. https://doi.org/10.1002/cssc.201501401.
[91] SeptinaGunawan W, Ikeda S, Harada T, Higashi M, Abe R, Matsumura M. Photosplitting of water from wide-gap Cu(in,ga)S_2 thin films modified with a CdS layer and pt nanoparticles for a high-onset-potential photocathode. J Phys Chem C 2015;119:8576–83. https://doi.org/10.1021/acs.jpcc.5b02068.
[92] Yang W, Kim JH, Hutter OS, Phillips LJ, Tan J, Park J, Lee H, Major JD, Lee JS, Moon J. Benchmark performance of low-cost Sb2Se3 photocathodes for unassisted solar overall water splitting. Nat Commun 2020;11. https://doi.org/10.1038/s41467-020-14704-3.
[93] Zhang L, Minegishi T, Nakabayashi M, Suzuki Y, Seki K, Shibata N, Kubota J, Domen K. Durable hydrogen evolution from water driven by sunlight using (Ag, Cu)GaSe2 photocathodes modified with CdS and CuGa3Se5. Chem Sci 2015;6:894–901. https://doi.org/10.1039/C4SC02346C.
[94] Hu S, Lewis NS, Ager JW, Yang J, McKone JR, Strandwitz NC. Thin-film materials for the protection of semiconducting photoelectrodes in solar-fuel generators. J Phys Chem C 2015;119:24201–28. https://doi.org/10.1021/acs.jpcc.5b05976.
[95] Hodes G. Semiconductor and ceramic nanoparticle films deposited by chemical bath deposition. Phys Chem Chem Phys 2007;9:2181–96. https://doi.org/10.1039/b616684a.
[96] Nair PK, Nair MTS, Garcia VM, Arenas OL, Pen Y, Castillo A, Ayala IT, Gomezdaza O, Sánchez A, Campos J, Hu H, Suárez R, Rincón ME. Semiconductor thin films by chemical bath deposition for solar energy related applications. Sol Energy Mater Sol Cell 1998;52:313–44.
[97] Chalapathi U, Poornaprakash B, Park SH. Chemically deposited cubic SnS thin films for solar cell applications. Sol Energy 2016;139:238–48. https://doi.org/10.1016/j.solener.2016.09.046.
[98] Osuagwu B, Raza W, Tesler AB, Schmuki P. Facile approach of direct sulfidation of FTO to form vertically aligned SnS 2 nanoflake photoanodes for efficient photoelectrochemical water splitting. ACS Appl Energy Mater 2021;4:8395–400. https://doi.org/10.1021/acsaem.1c01615.
[99] Deng S, Chen Y, Li Q, Sun J, Lei Z, Hu P, Liu ZH, He X, Ma R. Direct growth of SnS2 nanowall photoanode for high responsivity self-powered photodetectors. Nanoscale 2022;14:14097–105. https://doi.org/10.1039/d2nr03201e.
[100] Zhang K, Zhang R, Xia W, Sun H, He J, Zeng X, Li T. Photocatalytic performance for palm-fiber-like SnS2 nanoflakes with full solar spectrum light response. Appl Surf Sci 2022;605:154642. https://doi.org/10.1016/j.apsusc.2022.154642.
[101] Osuagwu B, Raza W, Tesler AB, Schmuki P. Facile approach of direct sulfidation of FTO to form vertically aligned SnS 2 nanoflake photoanodes for efficient photoelectrochemical water splitting. ACS Appl Energy Mater 2021;4:8395–400. https://doi.org/10.1021/acsaem.1c01615.
[102] Lin J, Liu Y, Liu Y, Huang C, Liu W, Mi X, Fan D, Fan F, Lu H, Chen X. SnS 2 nanosheets/H-TiO 2 nanotube arrays as a type II heterojunctioned photoanode for photoelectrochemical water splitting. ChemSusChem 2019;12:961–7. https://doi.org/10.1002/cssc.201802691.

[103] Hu W, Quang ND, Majumder S, Park E, Kim D, Choi HS, Chang HS. Efficient photo charge transfer of Al-doped ZnO inverse opal shells in SnS2 photoanodes prepared by atomic layer deposition. J Alloys Compd 2020;819:153349. https://doi.org/10.1016/j.jallcom.2019.153349.
[104] Wei R, Hu J, Zhou T, Zhou X, Liu J, Li J. Ultrathin SnS2 nanosheets with exposed {0 0 1} facets and enhanced photocatalytic properties. Acta Mater 2014;66:163–71. https://doi.org/10.1016/j.actamat.2013.11.076.
[105] Zuo Y, Liu Y, Li J, Du R, Yu X, Xing C, Zhang T, Yao L, Arbiol J, Llorca J, Sivula K, Guijarro N, Cabot A. Solution-processed ultrathin SnS 2 -Pt nanoplates for photoelectrochemical water oxidation. ACS Appl Mater Interfaces 2019;11:6918–26. https://doi.org/10.1021/acsami.8b17622.
[106] Joshi MP, Khot KV, Patil SS, Mali SS, Hong CK, Bhosale PN. Investigating the light harvesting capacity of sulfur ion concentration dependent SnS2 thin films synthesized by self-assembled arrested precipitation technique. Mater Res Express 2019;6. https://doi.org/10.1088/2053-1591/ab25c6.
[107] Ahmet IY, Guc M, Sánchez Y, Neuschitzer M, Izquierdo-Roca V, Saucedo E, Johnson AL. Evaluation of AA-CVD deposited phase pure polymorphs of SnS for thin films solar cells. RSC Adv 2019;9:14899–909. https://doi.org/10.1039/c9ra01938c.
[108] Guc M, Andrade-Arvizu J, Ahmet IY, Oliva F, Placidi M, Alcobé X, Saucedo E, Pérez-Rodríguez A, Johnson AL, Izquierdo-Roca V. Structural and vibrational properties of α- and π-SnS polymorphs for photovoltaic applications. Acta Mater 2020;183:1–10. https://doi.org/10.1016/j.actamat.2019.11.016.
[109] Ould Salem M, Fonoll R, Giraldo S, Sanchez Y, Placidi M, Izquierdo-Roca V, Malerba C, Valentini M, Sylla D, Thomere A, Ahmedou DO, Saucedo E, Pérez-Rodríguez A, Jehl Li-Kao Z. Over 10% efficient wide bandgap CIGSe solar cells on transparent substrate with Na predeposition treatment. Solar RRL 2000284 2020:1–7. https://doi.org/10.1002/solr.202000284.
[110] Caballero R, Condé V, León M. SnS thin films grown by sulfurization of evaporated Sn layers: effect of sulfurization temperature and pressure. Thin Solid Films 2016;612:202–7. https://doi.org/10.1016/j.tsf.2016.06.018.
[111] Cao M, Yao K, Wu C, Huang J, Yang W, Zhang L, Lei F, Sun Y, Wang L, Shen Y. Facile synthesis of SnS and SnS2 nanosheets for FTO/SnS/SnS2/Pt photocathode. ACS Appl Energy Mater 2018;1:6497–504. https://doi.org/10.1021/acsaem.8b01414.
[112] Wu F, Wang Z, Zhang C, Luo B, Xiao M, Wang S, Du A, Li L, Wang L. Two-dimensional heterojunction SnS2/SnO2 photoanode with excellent photoresponse up to near infrared region. Sol Energy Mater Sol Cell 2020;207:110342. https://doi.org/10.1016/j.solmat.2019.110342.
[113] Osuagwu B, Raza W, Tesler AB, Schmuki P. Facile approach of direct sulfidation of FTO to form vertically aligned SnS2Nanoflake photoanodes for efficient photoelectrochemical water splitting. ACS Appl Energy Mater 2021;4:8395–400. https://doi.org/10.1021/acsaem.1c01615.
[114] Guc M, Caballero R, Lisunov KG, López N, Arushanov E, Merino JM, León M. Disorder and variable-range hopping conductivity in Cu 2ZnSnS4 thin films prepared by flash evaporation and post-thermal treatment. J Alloys Compd 2014;596:140–4. https://doi.org/10.1016/j.jallcom.2014.01.177.
[115] Chalapathi U, Poornaprakash B, Park SH. Enhanced mobility of Cu4SnS4 films prepared by annealing SnS–CuS stacks in a graphite box. Sol Energy 2017;155:336–41. https://doi.org/10.1016/j.solener.2017.06.051.
[116] Lindwall G, Shang SL, Kelly NR, Anderson T, Liu ZK. Thermodynamics of the S-Sn system: implication for synthesis of earth abundant photovoltaic absorber materials. Sol Energy 2016;125:314–23. https://doi.org/10.1016/j.solener.2015.12.013.
[117] Reddy KTR, Reddy PP. Structural studies on SnS films grown by a two-stage process. Mater Lett 2002;56:108–11.
[118] Malaquias J, Fernandes PA, Salomé PMP, Da Cunha AF. Assessment of the potential of tin sulphide thin films prepared by sulphurization of metallic precursors as cell absorbers. Thin Solid Films 2011;519:7416–20. https://doi.org/10.1016/j.tsf.2011.01.393.
[119] Xia W, Wang H, Zeng X, Han J, Zhu J, Zhou M, Wu S. High-efficiency photocatalytic activity of type II SnO/Sn3O 4 heterostructures via interfacial charge transfer. CrystEngComm 2014;16:6841–7. https://doi.org/10.1039/c4ce00884g.
[120] Smith AJ, Meek PE, Liang WY. Raman scattering studies of SnS2, and SnSe2. J Phys C Solid State Phys 1977;10:1321–33. http://iopscience.iop.org/0022-3719/10/8/035.
[121] Barone G, Hibbert TG, Mahon MF, Molloy KC, Price LS, Parkin IP, Hardy AME, Field MN. Deposition of tin sulfide thin films from tin(IV) thiolate precursors. J Mater Chem 2001;11:464–8. https://doi.org/10.1039/b005888m.
[122] Yu D, Liu Y, Sun L, Wu P, Zhou W. Density functional study on the hole doping of single-layer SnS2 with metal element X (X = Li, Mg, and Al). Phys Chem Chem Phys 2016;18:318–24. https://doi.org/10.1039/c5cp05069c.
[123] Sinsermsuksakul P, Heo J, Noh W, Hock AS, Gordon RG. Atomic layer deposition of tin monosulfide thin films. Adv Energy Mater 2011;1:1116–25. https://doi.org/10.1002/aenm.201100330.